The Astrophysical Journal Letters, 847:L18 (7pp), 2017 October 1 https://doi.org/10.3847/2041-8213/aa8bff

Three Statistically Validated *K2* Transiting Warm Jupiter Exoplanets Confirmed as Low-mass Stars

Avi Shporer[1], George Zhou[2], Andrew Vanderburg[2,7], Benjamin J. Fulton[1], Howard Isaacson[3], Allyson Bieryla[2], Guillermo Torres[2], Timothy D. Morton[4], Joao Bento[5], Perry Berlind[2], Michael L. Calkins[2], Gilbert A. Esquerdo[2], Andrew W. Howard[6], and David W. Latham[2]

[1] Division of Geological and Planetary Sciences, California Institute of Technology, Pasadena, CA 91125, USA
[2] Harvard-Smithsonian Center for Astrophysics, 60 Garden Street, Cambridge, MA 02138, USA
[3] Astronomy Department, University of California, Berkeley, CA, USA
[4] Department of Astrophysical Sciences, Princeton University, Princeton, NJ 08544, USA
[5] Research School of Astronomy and Astrophysics, Mount Stromlo Observatory, Australian National University, Weston, ACT 2611, Australia
[6] Department of Astronomy, California Institute of Technology, Pasadena, CA, USA
Received 2017 August 5; revised 2017 September 7; accepted 2017 September 11; published 2017 September 27

Abstract

We have identified three *K2* transiting star–planet systems, K2-51 (EPIC 202900527), K2-67 (EPIC 206155547), and K2-76 (EPIC 206432863), as stellar binaries with low-mass stellar secondaries. The three systems were statistically validated as transiting planets, and through measuring their orbits by radial velocity (RV) monitoring we have derived the companion masses to be $0.1459^{+0.0029}_{-0.0032}$ $M_{\odot}$ (EPIC 202900527 B), $0.1612^{+0.0072}_{-0.0067}$ $M_{\odot}$ (EPIC 206155547 B), and 0.0942 ± 0.0019 $M_{\odot}$ (EPIC 206432863 B). Therefore, they are not planets but small stars, part of the small sample of low-mass stars with measured radius and mass. The three systems are at an orbital period range of 12–24 days, and the secondaries have a radius within 0.9–1.9 $R_{\rm J}$, not inconsistent with the properties of warm Jupiter planets. These systems illustrate some of the existing challenges in the statistical validation approach. We point out a few possible origins for the initial misclassification of these objects, including poor characterization of the host star, the difficulty in detecting a secondary eclipse in systems on an eccentric orbit, and the difficulty in distinguishing between the smallest stars and gas giant planets as the two populations have indistinguishable radius distributions. Our work emphasizes the need for obtaining medium-precision RV measurements to distinguish between companions that are small stars, brown dwarfs, and gas giant planets.

Key words: binaries: eclipsing – stars: individual (K2-51, EPIC 202900527, K2-67, EPIC 206155547, K2-76, EPIC 206432863)

1. Introduction

Space-based surveys (*Kepler*, Borucki 2016; *K2*, Howell et al. 2014) are producing an increasing number of transiting planet candidates (e.g., Coughlin et al. 2016; Crossfield et al. 2016; Vanderburg et al. 2016). Those candidates need to be examined by gathering additional data, to check whether the transit light curve is produced by a transiting star–planet system, or by a different scenario, making the object a false positive (e.g., Torres et al. 2011; Fressin et al. 2013). As there are insufficient observational resources needed for gathering the amount of data required to investigate the true nature of each transiting planet candidate, and because some planets cannot be confirmed with current observational capabilities, a *statistical validation* approach was developed (e.g., Torres et al. 2011, 2015; Morton et al. 2016). This approach uses a relatively small amount of observational follow-up data, typically including a single spectrum and a single high angular resolution image of the target, and is based on estimating the probability that the transit light curve is produced by a transiting star–planet system and not a false-positive scenario (e.g., Torres et al. 2011; Morton 2012).

Therefore, instead of the traditional approach of confirming a transiting planet candidate by measuring its orbit and deriving its mass, the validation approach puts an upper limit on the probability that the candidate is a false positive. That upper limit is typically at the 1% or 0.1% level in order to declare a candidate as a validated planet (e.g., Montet et al. 2015; Crossfield et al. 2016; Morton et al. 2016). Hence, the validated planets have measured orbital periods and radii, but their masses are unknown.

As part of a campaign to determine masses of transiting warm Jupiter planets—gas giant planets receiving stellar irradiation below about 10^8 erg s^{-1} cm^{-2}, equivalent to orbits beyond about 10 days around Sun-like stars (Shporer et al. 2017)—we have measured the masses of three of the *K2* validated planets. The resulting masses are in the range of 0.09–0.16 $M_{\odot}$; therefore, they are not planets but small stars. Those systems are EPIC 202900527 (K2-51), EPIC 206155547 (K2-67), and EPIC 206432863 (K2-76), validated by Crossfield et al. (2016).

We describe our *K2* data processing and gathering of spectroscopic data in Section 2. The data analysis is described in Section 3. In Section 4, we discuss our findings and briefly explore possible reasons for the misclassification of these stellar binaries as planetary systems. Throughout the text we refer to the transit interchangeably as the primary eclipse. Although the three systems have *K2* numbers (e.g., K2-51), we refer to them hereafter by their EPIC ID number (e.g., EPIC 202900527) since the former is reserved for planetary systems. In addition, we refer to the low-mass secondary in each system using the upper case "B" (e.g., EPIC 202900527 B) since it is a stellar object.

[7] National Science Foundation Graduate Research Fellow.

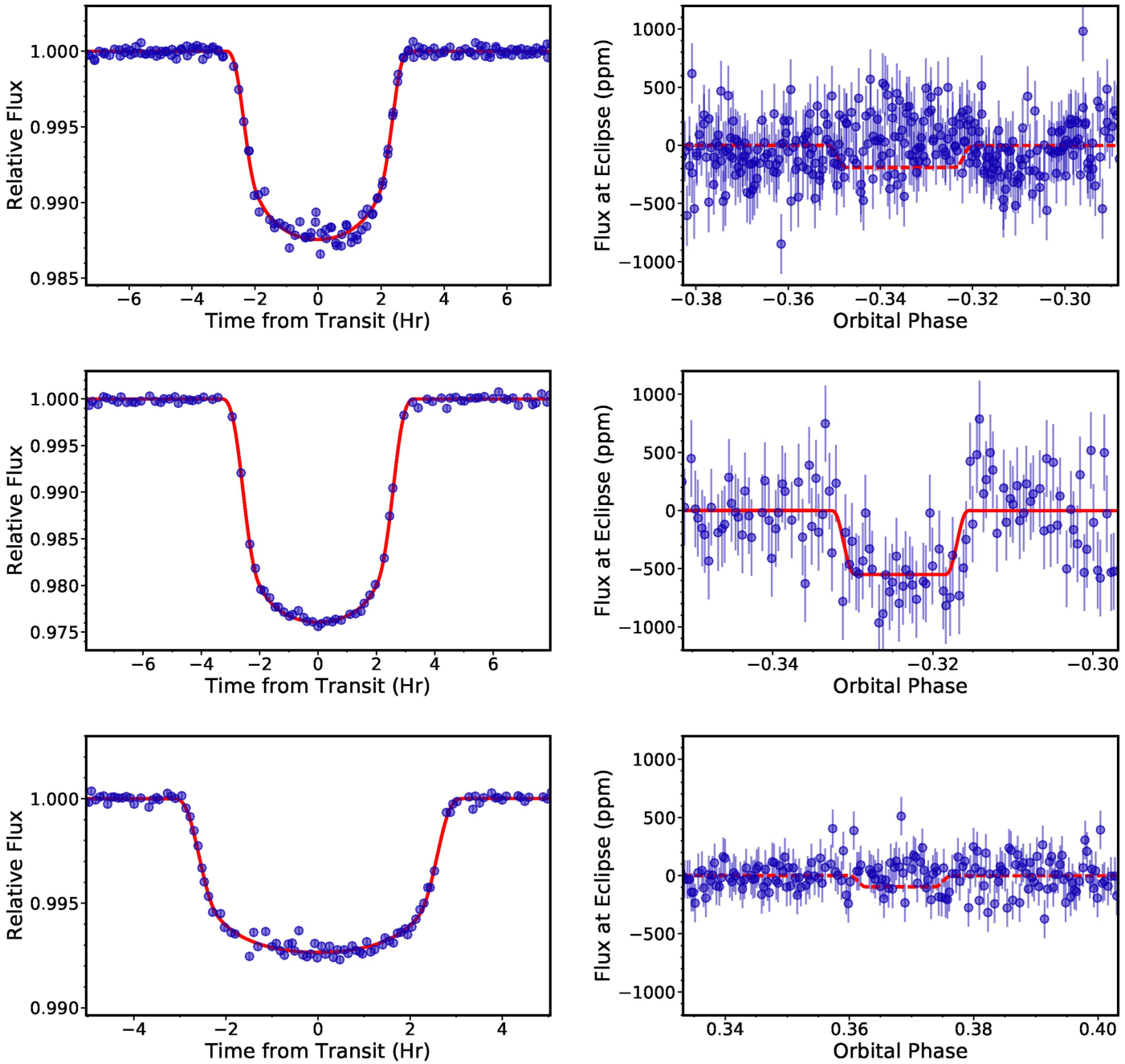

Figure 1. Normalized and phase-folded *K2* light curves of the transit (left column) and secondary eclipse (right column; plotted in ppm) of EPIC 202900527 (top row), EPIC 206155547 (middle row), and EPIC 206432863 (bottom row). *K2* measurements are in blue, and the fitted model is plotted with a solid red line for the three transits and the secondary eclipse of EPIC 206155547. For EPIC 202900527 and EPIC 206432863 the plotted secondary eclipse models show the 3σ upper limit on the eclipse depth, plotted with a dashed red line. All measurements are plotted with error bars, which in the transit light curve panels are smaller than the marker size.

2. Observations

2.1. K2

The three targets were observed by *K2* during Campaign 2 (EPIC 202900527) and Campaign 3 (EPIC 206155547 and EPIC 206432863), in long cadence (29.4 minute integration time). We reduced the *K2* light curves following Vanderburg & Johnson (2014) and Vanderburg et al. (2016). Upon identifying the transits we re-processed the light curves by simultaneously fitting for the transits, *K2* thruster systematics, and low-frequency variations as described by Vanderburg et al. (2016). The phase-folded light curves are plotted in Figure 1.

2.2. Keck/HIRES

The Keck/HIRES data analyzed and presented here include 20 spectra at a resolution of $R \sim 60{,}000$. We obtained 7 spectra of EPIC 206155547 and 13 of EPIC 206432863, during 18 nights from 2015 August 1 UT to 2017 June 28 UT. We have also obtained a Keck/HIRES spectrum of EPIC 202900527, used only for spectroscopic characterization of the primary star

Table 1
Radial Velocities

Time BJD	RV (km s^{-1})	RV Error (km s^{-1})
EPIC 202900527—FLWO 1.5 m/TRES		
2457168.87299	−17.812	0.089
2457852.92588	3.141	0.090
2457853.95594	7.154	0.065
2457854.95084	0.000	0.090
2457863.93643	−6.752	0.090
2457864.95402	−20.111	0.175
2457906.81976	2.089	0.122
2457907.79475	−9.658	0.074
2457908.80884	−15.654	0.062
2457909.80521	−17.658	0.138
2457914.78970	−11.337	0.182
EPIC 206155547—Keck/HIRES		
2457354.82966	34.953	0.276
2457652.05475	33.550	0.258
2457654.00564	35.045	0.367
2457887.11446	51.393	0.231
2457907.09022	51.378	0.637
2457908.08529	54.720	0.108
2457909.09961	56.853	0.040
EPIC 206432863—Keck/HIRES		
2457236.12417	−11.776	0.115
2457652.97550	0.658	0.577
2457653.99404	−1.006	0.103
2457678.89215	−5.313	0.051
2457713.86465	−0.755	0.072
2457747.76545	0.362	0.205
2457760.73066	0.791	0.095
2457887.10573	−10.511	0.122
2457910.10825	−13.870	0.052
2457913.08178	−4.266	0.244
2457926.10787	−1.742	0.103
2457927.13167	0.076	0.212
2457933.02457	−16.261	0.144

and not for radial velocity (RV) measurement (see Sections 2.3 and 3.1).

We used the Keck/HIRES instrumental setup of the California Planet Search (Howard et al. 2009). Since we can tolerate a medium RV precision of ∼0.1 km s^{-1}, we used the so-called telluric lines method where the iodine cell is removed from the light path (see, e.g. Shporer et al. 2016, their Section 2.2). Briefly, a wavelength solution is obtained through a nightly exposure of a Thorium–Argon lamp and the RVs are derived by measuring the offset in the position of the telluric absorption bands in the target spectra and that of a reference B-type star (Chubak et al. 2012). The RV due to Earth's barycentric motion is then removed, resulting in the target's absolute systemic velocity (Nidever et al. 2002; Chubak et al. 2012).

We used exposure times of 1.5–20 minutes, depending on target brightness, and the spectra we obtained have a signal-to-noise ratio (S/N) of 20–40 per pixel. Keck/HIRES RV measurements are listed in Table 1, and the phase-folded RV curves of EPIC 206155547 and EPIC 206432863 are shown in Figure 2.

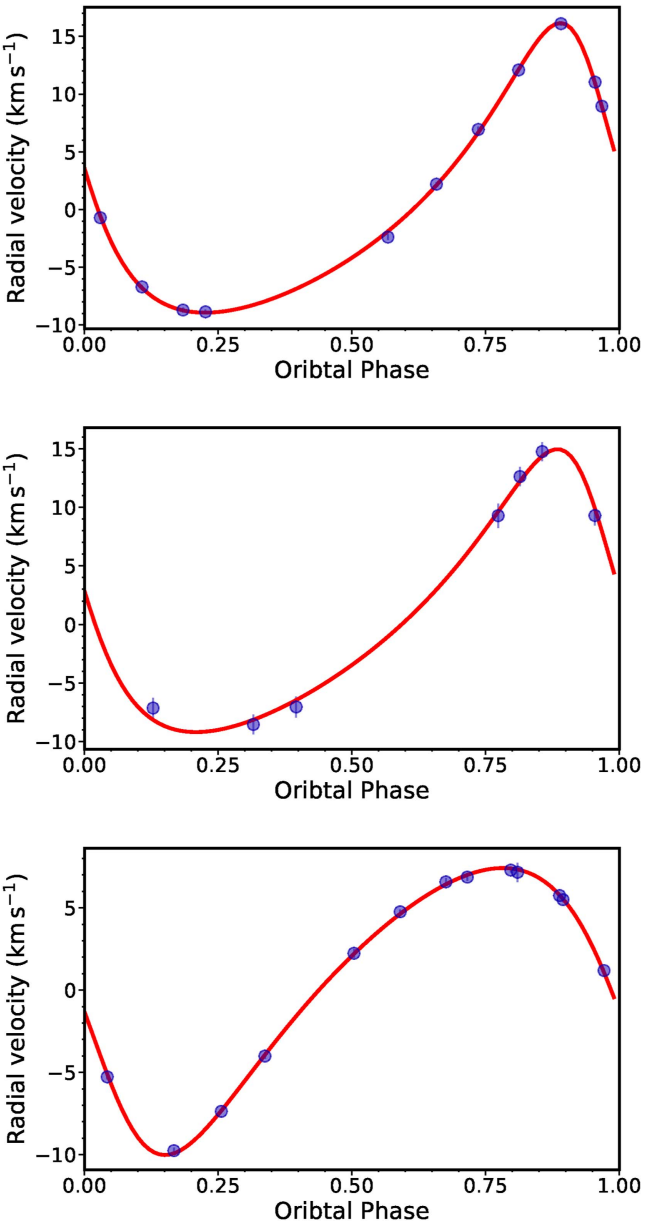

Figure 2. Phase-folded RV curves, after subtracting the RV zero-point γ, of EPIC 202900527 (top panel), EPIC 206155547 (middle panel), and EPIC 206432863 (bottom panel). The transit is at phase zero. RVs are marked in blue, and the fitted orbit models are marked as solid red lines. All measurements are plotted with error bars that are often smaller than the marker size.

2.3. Fred Lawrence Whipple Observatory (FLWO) 1.5 m/TRES

We obtained 11 spectra of EPIC 202900527 using the Tillinghast Reflector Echelle Spectrograph (TRES; Fűrész 2008) at the FLWO 1.5 m telescope on Mount Hopkins, Arizona. The TRES spectra have a resolution of $R \sim 44{,}000$ and were collected between 2015 May 26 UT and 2017 June 10 UT. We used exposure times between 22 and 34 minutes, which resulted in an S/N per resolution element of 17–29.

We reduced and extracted the TRES spectra as described by Buchhave et al. (2010). We derived the RVs by cross correlating each spectrum order by order against the observed spectrum with the highest S/N in the wavelength range of

4520–6280 Å. EPIC 202900527 11 TRES RVs are listed in Table 1, and the phase-folded RV curve is shown in Figure 2.

The reference (or template) spectrum is at BJD = 2457854.95084 and its RV is listed as 0.0 km s^{-1} in Table 1. To allow putting the TRES RVs on an absolute scale, we determined the template spectrum absolute RV by cross correlating it with a synthetic spectrum to be -57.87 ± 0.10 km s^{-1}. This RV offset is not added to the RVs in Table 1 to avoid inflating their uncertainties.

3. Data Analysis and Results

3.1. Stellar Spectroscopic Parameters

We derived the spectroscopic stellar parameters using the `SpecMatch` package (Petigura 2015; Petigura et al. 2017) and the iodine-free HIRES spectra of each star. Those include the effective temperature $T_{\rm eff}$, surface gravity $\log g$, metallicity [Fe/H], and stellar rotation projected on the line of sight $V \sin(I)$, where V is the equatorial rotation and I is the stellar rotation inclination angle. We averaged the parameters extracted from all of the individual observations. The observation-to-observation parameter variance was smaller than the quoted 1σ uncertainties in all cases. The `SpecMatch` results are listed in Table 2.

3.2. Global Model Fitting

We performed a global modeling of the available photometric and RV measurements, along with the spectroscopic atmospheric properties of the primary star, to derive the parameters for each system. For stellar binaries, the transit-derived orbital semimajor axis normalized by the primary stellar radius a/R_1 is dependent on the sum of the two components' masses $M_1 + M_2$ and the volume of the primary star, as per Sozzetti et al. (2007):

$$\left(\frac{a}{R_1}\right)^3 = \frac{G}{4\pi^2} P^2 \frac{M_1 + M_2}{R_1^3}, \quad (1)$$

where P is the orbital period and G the gravitational constant. To take advantage of this relation, we fit directly for the masses of the two stars, the primary radius, and the secondary-to-primary radii ratio R_2/R_1, as well as the standard transit and RV orbital parameters including the orbital period P, mid-transit time T_0, line-of-sight orbital inclination i, orbital eccentricity parameters $\sqrt{e}\cos\omega$ and $\sqrt{e}\sin\omega$ (where e is the orbital eccentricity and ω the argument of periastron), RV zero-point γ, RV jitter s, and the primary metallicity [Fe/H]. We include the secondary eclipse in our model, where the eclipse depth is the secondary-to-primary flux ratio in the *Kepler* band (F_2/F_1). We used the model of Mandel & Agol (2002) for the transit and secondary eclipse light curves.

At each iteration we use the trial masses and eccentricity to calculate the normalized orbital semimajor axis a/R_1, as per Equation (1), and an orbital RV semi-amplitude K. To constrain the stellar masses and radii we interpolate the Dartmouth isochrones (Dotter et al. 2008) at each step over the parameters M_1, R_1, and [Fe/H], to derive an expected $T_{\rm eff}$ value. We then compare the isochrone-derived $T_{\rm eff}$ with that measured spectroscopically and add the difference as a penalty term to the likelihood function. We apply a similar penalty in the likelihood function for the primary star's $\log g$ value, calculated from the tested M_1 and R_1 values, by comparing it to that measured spectroscopically. The stellar metallicity [Fe/H] is constrained by a Gaussian prior over its spectroscopically measured value. The remaining parameters are assumed to have uniform priors. The RV jitter s is calculated as per Haywood et al. (2016).

Quadratic limb-darkening coefficients, u_1 and u_2, are interpolated from Claret (2004) to the atmospheric parameters of each star and are held fixed during the fitting process.

We explore the posterior probability distributions via a Markov Chain Monte Carlo analysis, using the affine invariant ensemble sampler *emcee* (Foreman-Mackey et al. 2013). The 68.3% confidence regions for the MCMC free parameters, as well as several inferred parameters, are listed in Table 2. The inferred parameters include, in addition to parameters mentioned above, *Kepler* band luminosity of the primary L_1, and the secondary L_2, system age, impact parameter of the transit b, and of the secondary eclipse (occultation) $b_{\rm occ}$, transit duration T_{14}, ingress duration T_{12}, and secondary eclipse phase where primary eclipse (transit) phase is taken as phase zero. The best-fit transit and secondary eclipse light curve models are shown in Figure 1 and the orbital RV curve models in Figure 2.

For the most part the transit parameters we derive are similar to those reported by Crossfield et al. (2016). One notable exception is the orbital period of EPIC 206432863. We find that the true orbital period is exactly half the one reported by those authors. Another difference is our detection of a secondary eclipse for EPIC 206155547, at a depth of 560^{+160}_{-180} ppm. For EPIC 202900527 and EPIC 206432863 we find no detectable secondary eclipses, and we place 3σ upper limits on their depths of 190 and 97 ppm, respectively.

4. Discussion

The three objects studied here, EPIC 202900527 B, EPIC 206155547 B, and EPIC 206432863 B, are among the smallest stars with measured radius and mass. Strictly speaking, the values are model-dependent to some extent as they rely on masses and radii for the primary stars inferred from stellar evolution models. The uncertainties in the host star properties dominate the error budget for the secondaries. The positions of the B components in the radius–mass diagram are shown in Figure 3, compared to other objects ranging from massive planets to brown dwarfs and small stars (Pont et al. 2005, 2006; Southworth 2011; Tal-Or et al. 2011; Ofir et al. 2012; Akeson et al. 2013; Díaz et al. 2013, 2014; Moutou et al. 2013; Triaud et al. 2013; Zhou et al. 2014; Bayliss et al. 2017; von Boetticher et al. 2017). The overplotted lines are theoretical solar metallicity radius–mass relations (Baraffe et al. 2003, 2015). While EPIC 202900527 B agrees well with the theoretical prediction, EPIC 206155547 B appears to be larger than predicted for its mass, and EPIC 206432863 B appears to be smaller than predicted for its mass. In fact, EPIC 206432863 B is one of the smallest objects with mass just above the theoretical minimum mass required for hydrogen burning, where the behavior of the radius changes from slowly *decreasing* with increasing mass for massive brown dwarfs, to *increasing* with increasing mass for low-mass stars.

As far as we are aware there are no publicly available model predictions over the full mass range shown in Figure 3 for metallicities other than solar. However, the discrepancy for EPIC 206432863 B does not appear to be due to metallicity, as our spectroscopic analysis indicates it has [Fe/H] = $+0.01 \pm 0.04$, essentially matching the metallicity of the models shown in the figure. Similarly, metallicity is unlikely to explain the

Table 2
Fitted and Derived Parameters

Parameter	EPIC 202900527 (K2-51)			EPIC 206155547 (K2-67)			EPIC 206432863 (K2-76)		
	Value	$+1\sigma$	-1σ	Value	$+1\sigma$	-1σ	Value	$+1\sigma$	-1σ
Spectroscopic parameters[a]									
$T_{\rm eff}$ (K)	5548	60	60	5907	60	60	5762	60	60
$\log g$ (cgs)	4.17	0.07	0.07	4.13	0.07	0.07	4.20	0.07	0.07
[Fe/H]	+0.32	0.04	0.04	−0.32	0.04	0.04	+0.01	0.04	0.04
$V \sin(I)$ (km s^{-1})	11.4	0.5	0.5	<2	⋯	⋯	5.3	1.8	1.8
Fitted parameters[b]									
P (day)	13.00847	0.00027	0.00018	24.38752	0.00072	0.00067	11.98980	0.00017	0.00018
$T_0-2456900$ (BJD)	5.75715	0.00069	0.00090	85.88408	0.00094	0.00086	83.82617	0.00055	0.00054
M_1 ($M_\odot$)	1.068	0.029	0.032	0.916	0.031	0.029	0.964	0.026	0.026
R_1 ($R_\odot$)	1.695	0.049	0.037	1.399	0.079	0.056	1.171	0.060	0.033
M_2 ($M_\odot$)	0.1459	0.0029	0.0032	0.1612	0.0072	0.0067	0.0942	0.0019	0.0019
R_2/R_1	0.10047	0.00066	0.00065	0.14261	0.00130	0.00087	0.07843	0.00081	0.00046
i (deg)	89.98	1.08	0.97	89.37	0.43	0.52	89.35	0.43	0.42
$\sqrt{e}\cos\omega$	0.403	0.010	0.016	0.452	0.016	0.017	−0.4081	0.0104	0.0098
$\sqrt{e}\sin\omega$	0.4656	0.0078	0.0106	0.397	0.040	0.044	−0.2971	0.0104	0.0098
γ[c] (km s^{-1})	−8.945	0.082	0.081	42.09	0.36	0.36	−6.506	0.050	0.053
Jitter s (km s^{-1})	0.170	0.150	0.090	0.81	0.40	0.36	0.107	0.070	0.056
[Fe/H]	+0.325	0.045	0.042	−0.318	0.043	0.044	+0.010	0.041	0.038
u_1[d]	0.4714	⋯	⋯	0.3272	⋯	⋯	0.3921	⋯	⋯
u_2[d]	0.2185	⋯	⋯	0.2971	⋯	⋯	0.2630	⋯	⋯
F_2/F_1[e] (ppm)	<190	⋯	⋯	560	160	180	<97	⋯	⋯
Derived parameters									
R_2 ($R_\odot$)	0.1702	0.0046	0.0032	0.1996	0.0119	0.0067	0.0913	0.0048	0.0026
K (km s^{-1})	12.53	0.10	0.10	12.00	0.14	0.14	8.720	0.069	0.074
a/R_1	14.66	0.23	0.33	25.80	0.98	1.06	19.17	0.52	0.89
$T_{\rm eff}$ (K)	5579	77	78	5908	64	63	5747	70	64
$\log g$ (cgs)	4.01	0.011	0.015	4.104	0.024	0.038	4.288	0.033	0.020
L_1 ($L_\odot$)	2.52	0.39	0.22	2.17	0.31	0.22	1.36	0.13	0.12
L_2 ($L_\odot$)[e]	<0.00010	⋯	⋯	0.00114	0.00037	0.00043	<0.00011	⋯	⋯
Age (Gyr)	8.49	0.97	1.35	10.4	1.2	1.0	9.16	0.93	0.91
a (au)	0.11545	0.00091	0.00087	0.1687	0.0017	0.0017	0.10439	0.00093	0.00090
b	0.118	0.119	0.082	0.20	0.15	0.14	0.24	0.14	0.16
T_{14} (day)	0.2222	0.0016	0.0014	0.2533	0.0031	0.0022	0.2380	0.0020	0.0013
T_{12} (day)	0.02051	0.00102	0.00034	0.03276	0.0034	0.0013	0.0183	0.0021	0.0010
e	0.3797	0.0058	0.0090	0.360	0.016	0.018	0.2545	0.0065	0.0070
ω (deg)	40.7	1.1	1.7	48.6	3.9	3.6	−126.1	1.5	1.5
Occultation Phase[f]	0.6579	0.0048	0.0076	0.6764	0.0015	0.0021	0.3692	0.0046	0.0047
$b_{\rm occ}$	0.20	0.22	0.14	0.33	0.24	0.22	0.18	0.10	0.12

Notes.
[a] Derived using `SpecMatch` analysis of the spectra.
[b] Model fit parameters, fitted to the *K2* light curve, RVs, and stellar isochrones. Gaussian priors are applied to [Fe/H] using the values derived from the `SpecMatch` spectroscopic analysis. See Section 3 for more information.
[c] For EPIC 206155547 and EPIC 206432863 γ is the binary system's center of mass RV since the HIRES RVs are on an absolute scale. For EPIC 202900527 the RV of the template spectrum (-57.87 ± 0.10 km s^{-1}; see Section 2.3) needs to be added to γ to get the center of mass RV.
[d] Parameter fixed during the model fitting process.
[e] 3σ upper limit given when no eclipse was detected.
[f] The transit, or primary eclipse, is at phase zero.

inflated radius of EPIC 206155547 B, as this system is metal-poor and available model predictions over this mass range indicate that if anything the effect should go in the opposite direction, making the star smaller (e.g. Burrows et al. 2011). In principle, stellar activity remains a possible explanation for the larger size, as has been found to be the case in many other low-mass binaries (e.g., Torres 2013), though in most of those examples the activity is maintained at a high level by tidally induced rapid rotation in short period orbits (typically a few days). This is not expected in EPIC 206155547 given its longer period of 24 days and old age (≈10 Gyr).

The orbits of the three binary systems are moderately eccentric, with precisely measured eccentricities ranging from 0.25 to 0.38. Given their long orbital periods of 12–24 days they are not expected to have been tidally circularized within the stellar lifetime (e.g., Mazeh 2008), and the eccentricities are within the range seen in systems with a similar period range (see, e.g., Mazeh 2008, Figure 1; Shporer et al. 2016, Figure 6).

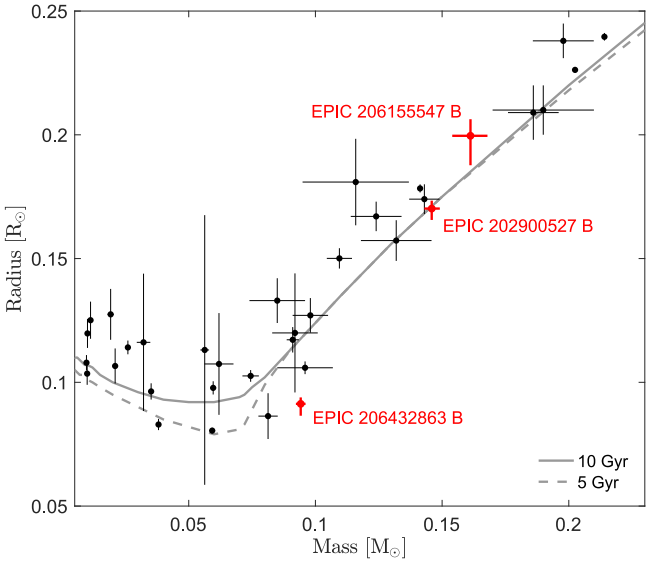

Figure 3. Radius–mass diagram for massive planets, brown dwarfs, and small stars. The three objects studied here are marked in red. The solid and dashed lines are theoretical radius–mass relations for 10 Gyr (solid line) and 5 Gyr (dashed line) old stars (Baraffe et al. 2015) and substellar objects (Baraffe et al. 2003) with solar metallicity.

4.1. Why Were These Stellar Binaries Classified as Transiting Planets?

The three systems discussed here were validated as planets by Crossfield et al. (2016) based on a statistical procedure that considered possible false-positive scenarios. That statistical validation procedure results in the relative likelihoods of the transit signals being due to a false positive or a true planet. The reported false-positive probabilities (FPPs) were $\sim 10^{-3}$ for the EPIC 202900527 and EPIC 206155547 systems and $\sim 10^{-4}$ for EPIC 206432863. Our identification of these objects as stellar binaries raises the question of why they were initially misclassified as planets.

For EPIC 202900527 and EPIC 206155547 the stellar companions' radii derived by Crossfield et al. (2016) are smaller than derived here by 30% and 20%, respectively. This is clearly one of the primary reasons for the low FPP estimated by Crossfield et al. (2016) for these two systems. The smaller companions' radii followed from a smaller estimate of the host star radius by 20% for both systems and a measured secondary-to-primary radii ratio that is 15% smaller for EPIC 202900527.

To investigate the origin of the smaller host star radii derived by Crossfield et al. (2016), we looked into their stellar characterization calculations (I. Crossfield 2017, private communication) using the *isochrones* package (Morton 2015a), which are then used by the *vespa* package (Morton 2015b) to calculate the FPPs. These calculations use optical spectra and broadband photometry, when available, from APASS, 2MASS, and *WISE*. We noticed that in these two cases the fitted stellar model is a poor fit to the data and is inconsistent with at least some of the input measurements. We believe this resulted from poor-quality broadband photometric measurements with underestimated uncertainties. Therefore, we conclude it is the host stars' poor characterization that led to the underestimated companion radii and the underestimated FPPs. Similar cases of poor stellar characterization can be identified by visually examining the *isochrone* output diagnostic plots or by calculating a goodness-of-fit metric.

The success of validation methods often relies on the ability to rule out the presence of secondary eclipses, which for systems with eccentric orbits, as those studied here, does not necessarily occur half an orbit away from the transit. While the procedure of Crossfield et al. (2016) did include a search for secondary eclipses throughout the entire orbital phase, it assumed an eclipse duration equal to that of the transit, which is usually not the case in eccentric systems. For EPIC 202900527, EPIC 206155547, and EPIC 206432863 the expected secondary eclipse durations are a factor of 1.66, 1.69, and 0.67 times the primary eclipse duration, respectively. As described in Section 3.2 we have searched for secondary eclipses as part of the global modeling. While we do not detect a secondary eclipse for EPIC 202900527 and EPIC 206432863, we do detect an eclipse for EPIC 206155547, the largest and most massive of the three objects, at close to 3σ significance. The measured eclipse depth of 560^{+160}_{-180} ppm is consistent with a stellar secondary and is at least an order of magnitude larger than the expected depth in case the secondary is substellar. The nondetection of this secondary eclipse by Crossfield et al. (2016) might be related to the fact that it is 1.69 times longer than the transit. Although, as noted earlier, the misclassification of EPIC 206155547 resulted from poor host star characterization, a detection of the secondary eclipse would have immediately led to classifying the companion as stellar.

We note that the radius distributions of large planets and small stars overlap, making it difficult for validation procedures to distinguish between the two kinds of objects. For EPIC 206432863 B this becomes especially difficult, since its mass of $0.0942 \pm 0.0019\ M_{\odot}$ ($=98.7 \pm 2.0\ M_{\rm J}$) is close to the theoretical minimal stellar mass required for burning hydrogen, and its radius of $0.0913^{+0.0048}_{-0.0026}\ R_{\odot}$ ($=0.888^{+0.047}_{-0.025}\ R_{\rm J}$) is fully consistent with radii of non-inflated planets. As shown in Figure 3 it is smaller than theoretically expected for its mass, making it further difficult to be identified as a stellar object through statistical validation. In addition, for EPIC 206432863 B Crossfield et al. (2016) report an orbital period that is twice the true value, which may have also affected the validation calculations.

5. Summary and Conclusions

We have identified three of the *K2* statistically validated warm Jupiter planets to be stellar binary systems with low-mass secondaries. We presented a few possible explanations for the misclassification, including poor host star characterization, the difficulty in identifying shallow secondary eclipses of long-period eccentric systems, and the difficulty to distinguish between small stars and gas giant planets. As a whole the misclassification of the three systems identified here presents the existing challenges in the validation approach, particularly when applied to long-period systems and/or gas giant planet candidates. Their correct classification, shown here (along with three other validated planets identified by Cabrera et al. 2017 as false positives), makes them good test cases for further improvement of statistical validation techniques of transiting planet candidates, which in turn will support current and future transiting planet surveys including *K2*, TESS (Sullivan et al. 2015), and PLATO (Rauer et al. 2014).

The medium-precision RVs we have obtained here, with a precision at the level of 0.1 km s^{-1}, exemplifies their efficiency in identifying transiting planet candidates where the transiting object is a low-mass star or a brown dwarf.

The three objects studied here belong to the small sample of low-mass stars with measured mass and radius. Further extending that sample will lead to a better understanding of small stars and the processes shaping their radius–mass relation.

A.V. is supported by the NSF Graduate Research Fellowship, grant No. DGE 1144152. G.T. acknowledges partial support for this work from NSF grant AST-1509375 and NASA grant NNX14AB83G (*Kepler* Participating Scientist Program). D.W.L. acknowledges partial support from the *Kepler* mission via Cooperative Agreement NNX13AB58A with the Smithsonian Astrophysical Observatory. This Letter includes data collected by the *K2* mission. Funding for the *K2* mission is provided by the NASA Science Mission directorate. Some of the data presented herein were obtained at the W. M. Keck Observatory, which is operated as a scientific partnership among the California Institute of Technology, the University of California, and the National Aeronautics and Space Administration. The Observatory was made possible by the generous financial support of the W. M. Keck Foundation.

Facilities: K2, Keck:I (HIRES), FLWO:1.5 m (TRES).

ORCID iDs

Avi Shporer https://orcid.org/0000-0002-1836-3120
Andrew Vanderburg https://orcid.org/0000-0001-7246-5438
Benjamin J. Fulton https://orcid.org/0000-0003-3504-5316
Howard Isaacson https://orcid.org/0000-0002-0531-1073
Guillermo Torres https://orcid.org/0000-0002-5286-0251
Michael L. Calkins https://orcid.org/0000-0002-2830-5661
Andrew W. Howard https://orcid.org/0000-0001-8638-0320
David W. Latham https://orcid.org/0000-0001-9911-7388

References

Akeson, R. L., Chen, X., Ciardi, D., et al. 2013, PASP, 125, 989
Baraffe, I., Chabrier, G., Barman, T. S., Allard, F., & Hauschildt, P. H. 2003, A&A, 402, 701
Baraffe, I., Homeier, D., Allard, F., & Chabrier, G. 2015, A&A, 577, A42
Bayliss, D., Hojjatpanah, S., Santerne, A., et al. 2017, AJ, 153, 15
Borucki, W. J. 2016, RPPh, 79, 036901
Buchhave, L. A., Bakos, G. A., Hartman, J. D., et al. 2010, ApJ, 720, 1118
Burrows, A., Heng, K., & Nampaisarn, T. 2011, ApJ, 736, 47
Cabrera, J., Barros, S. C. C., Armstrong, D., et al. 2017, A&A, in press (arXiv:1707.08007)
Chubak, C., Marcy, G., Fischer, D. A., et al. 2012, arXiv:1207.6212
Claret, A. 2004, A&A, 428, 1001
Coughlin, J. L., Mullally, F., Thompson, S. E., et al. 2016, ApJS, 224, 12
Crossfield, I. J. M., Ciardi, D. R., Petigura, E. A., et al. 2016, ApJS, 226, 7
Díaz, R. F., Damiani, C., Deleuil, M., et al. 2013, A&A, 551, L9
Díaz, R. F., Montagnier, G., Leconte, J., et al. 2014, A&A, 572, A109
Dotter, A., Chaboyer, B., Jevremović, D., et al. 2008, ApJS, 178, 89
Foreman-Mackey, D., Hogg, D. W., Lang, D., & Goodman, J. 2013, PASP, 125, 306
Fressin, F., Torres, G., Charbonneau, D., et al. 2013, ApJ, 766, 81
Fűrész, G. 2008, PhD thesis, Univ. Szeged
Haywood, R. D., Collier Cameron, A., Unruh, Y. C., et al. 2016, MNRAS, 457, 3637
Howard, A. W., Johnson, J. A., Marcy, G. W., et al. 2009, ApJ, 696, 75
Howell, S. B., Sobeck, C., Haas, M., et al. 2014, PASP, 126, 398
Mandel, K., & Agol, E. 2002, ApJL, 580, L171
Mazeh, T. 2008, in EAS Publ. Ser. 29, Tidal Effect in Stars, Planets and Disks, ed. M.-J. Goupil & J.-P. Zahn (Les Ulis: EDP Sciences), 1
Montet, B. T., Morton, T. D., Foreman-Mackey, D., et al. 2015, ApJ, 809, 25
Morton, T. D. 2012, ApJ, 761, 6
Morton, T. D. 2015a, isochrones: Stellar model grid package, Astrophysics Source Code Library, ascl:1503.010
Morton, T. D. 2015b, VESPA: False positive probabilities calculator, Astrophysics Source Code Library, ascl:1503.011
Morton, T. D., Bryson, S. T., Coughlin, J. L., et al. 2016, ApJ, 822, 86
Moutou, C., Bonomo, A. S., Bruno, G., et al. 2013, A&A, 558, L6
Nidever, D. L., Marcy, G. W., Butler, R. P., Fischer, D. A., & Vogt, S. S. 2002, ApJS, 141, 503
Ofir, A., Gandolfi, D., Buchhave, L., et al. 2012, MNRAS, 423, L1
Petigura, E. A. 2015, PhD thesis, Univ. California, Berkeley
Petigura, E. A., Howard, A. W., Marcy, G. W., et al. 2017, AJ, 154, 107
Pont, F., Melo, C. H. F., Bouchy, F., et al. 2005, A&A, 433, L21
Pont, F., Moutou, C., Bouchy, F., et al. 2006, A&A, 447, 1035
Rauer, H., Catala, C., Aerts, C., et al. 2014, ExA, 38, 249
Shporer, A., Fuller, J., Isaacson, H., et al. 2016, ApJ, 829, 34
Shporer, A., Zhou, G., Fulton, B. J., et al. 2017, ApJ, in press (arXiv:1708.07128)
Southworth, J. 2011, MNRAS, 417, 2166
Sozzetti, A., Torres, G., Charbonneau, D., et al. 2007, ApJ, 664, 1190
Sullivan, P. W., Winn, J. N., Berta-Thompson, Z. K., et al. 2015, ApJ, 809, 77
Tal-Or, L., Santerne, A., Mazeh, T., et al. 2011, A&A, 534, A67
Torres, G. 2013, AN, 334, 4
Torres, G., Fressin, F., Batalha, N. M., et al. 2011, ApJ, 727, 24
Torres, G., Kipping, D. M., Fressin, F., et al. 2015, ApJ, 800, 99
Triaud, A. H. M. J., Hebb, L., Anderson, D. R., et al. 2013, A&A, 549, A18
Vanderburg, A., & Johnson, J. A. 2014, PASP, 126, 948
Vanderburg, A., Latham, D. W., Buchhave, L. A., et al. 2016, ApJS, 222, 14
von Boetticher, A., Triaud, A. H. M. J., Queloz, D., et al. 2017, A&A, 604, L6
Zhou, G., Bayliss, D., Hartman, J. D., et al. 2014, MNRAS, 437, 2831